




Article

Graphene-Assembled Film-Based Reconfigurable Filtering Antenna with Enhanced Corrosion-Resistance

Yueyue Hui ^{1,†}, Haoran Zu ^{1,†}, Rongguo Song ^{1,*}, Huaqiang Fu ², Kaolin Luo ¹, Chao Tian ², Bian Wu ³ , Guan-Long Huang ⁴ , Zongkui Kou ⁵, Xin Cheng ^{6,*} and Daping He ^{1,*} 

- ¹ Hubei Engineering Research Center of RF-Microwave Technology and Application, School of Science, Wuhan University of Technology, Wuhan 430070, China; huiyueyue@whut.edu.cn (Y.H.); hrzu@stu.xidian.edu.cn (H.Z.); 261162@whut.edu.cn (K.L.)
- ² School of Materials Science and Engineering, Wuhan University of Technology, Wuhan 430070, China; fuhuaqiang@whut.edu.cn (H.F.); tian_chao@whut.edu.cn (C.T.)
- ³ The National Key Laboratory of Antennas and Microwave Technology, Xidian University, Xi'an 710071, China; bwu@mail.xidian.edu.cn
- ⁴ School of AI, Guangdong & Taiwan, Foshan University, Foshan 528225, China; hgl@fosu.edu.cn
- ⁵ State Key Laboratory of Advanced Technology for Materials Synthesis and Processing, Wuhan University of Technology, Wuhan 430070, China; zongkuikou@whut.edu.cn
- ⁶ Hubei Institute of Quality Supervision and Inspection, Wuhan 430061, China
- * Correspondence: rongguo_song@whut.edu.cn (R.S.); sharonxin@126.com (X.C.); hedaping@whut.edu.cn (D.H.)
- † These authors contributed equally to this work.

Abstract: Corrosion-resistance is the key to improve the reliability and service lifespan of highly integrated reconfigurable filtering antennae. However, the conventional methodology for corrosion prevention cannot achieve desired effects, due to the limited intrinsic corrosion-resistance capacity of traditional metal-based devices. Here, we developed a reconfigurable filtering antenna based on graphene assembled film (GAF), featuring significant corrosion-resistance enhancement. The GAF-based antenna exhibits comparable electrical performance when compared with a copper-based antenna, and can flexibly switch between two working modes, including ultra-wideband (UWB, 2.8–11 GHz) and narrowband filtering (NBF, 3.23–3.77 GHz). To further demonstrate the of the corrosion-resistance of GAF, a salt spray corrosion test found that the GAF-based antenna exhibits steady electrical properties after corrosion for over 336 h, while the copper-based antenna shows rapid performance degradation. The simulated and experimental results are in agreement, indicating that the proposed GAF reconfigurable filtering antenna can be applied to broader application prospects in communication systems, especially in severe environments.

Keywords: graphene antenna; corrosion resistance; graphene assembled film; reconfigurable filtering antenna; ultra-wideband



Citation: Hui, Y.; Zu, H.; Song, R.; Fu, H.; Luo, K.; Tian, C.; Wu, B.; Huang, G.-L.; Kou, Z.; Cheng, X.; et al. Graphene-Assembled Film-Based Reconfigurable Filtering Antenna with Enhanced Corrosion-Resistance. *Crystals* **2023**, *13*, 747. <https://doi.org/10.3390/cryst13050747>

Academic Editor: Andreas Thissen

Received: 10 April 2023

Revised: 26 April 2023

Accepted: 26 April 2023

Published: 29 April 2023



Copyright: © 2023 by the authors. Licensee MDPI, Basel, Switzerland. This article is an open access article distributed under the terms and conditions of the Creative Commons Attribution (CC BY) license (<https://creativecommons.org/licenses/by/4.0/>).

1. Introduction

The salient features of 5G mobile communication, such as high speed, large capacity, and low delay, put forward the requirements of miniaturization, integration, and multi-function for communication systems [1]. Filter and antenna, responsible for the selective filtering and receiving/transmitting of signals respectively, are usually designed independently, which enlarges the size of the radio frequency (RF) front-end and induces excessive insertion loss, due to the direct cascade of filter and antenna [2]. To solve these problems, filtering antennae, with filter and radiation functions, have received extensive attention [3,4]. In order to further improve integration, the reconfigurable filtering antenna has attracted much attention from antenna researchers [5–8]. The reconfigurable filtering antenna has the advantages of improving antenna selectivity, weakening external parasitic radiation/reception, and flexibly switching between different functions.

Meanwhile, the anti-corrosion ability of an antenna system is an important index in engineering applications, especially in high temperature and humidity environments [9–12]. With the development of communication systems, the number of antennae is increasing sharply. Due to the inherent properties of metal, the traditional metal-based antennae are readily corrodible, which not only causes great economic loss, but also has a negative impact on the performance and service life of the antennae. In the existing research, there are several traditional methods to improve the corrosion-resistance of antenna, which are radome [13,14], protective paints [15–18], optimizing the structure of the antenna, sacrificial anodes protection [19], and alloys with corrosion-resistance [20–23]. Radome and spray paint can protect the antenna from the impacts of the harsh environment, such as coastal cities [13–18]. Although those two methods are held in high regard in antennae anticorrosion, the introduction of radiation loss, high maintenance frequency, and low security are non-negligible shortcomings. Metal corrosion can be effectively reduced by reducing the part of the overlapping gap on the structure of the antenna. However, the disadvantages of this method are that corrosion-resistance is obtained by sacrificing the antenna performance and there are requirements for the infrastructure of an antenna. Sacrificial anode protections play an important role in metal protection, which have the advantages of easy installation and less maintenance, but the replacement of a failed anode is unaffordable [19]. Alloys with corrosion-resistance can also be used to protect an antenna from corrosion, such as stainless steel, titanium alloy, metal glass, etc., but these methods will lead to a reduction in the conductivity of the metal, which has a negative impact on the radiation efficiency of the antenna [20–23]. To sum up, it is urgent to develop new materials with good corrosion resistance and high electrical conductivity.

Graphene has significant advantages over conventional metal materials, in terms of flexibility, lightweight, thermal conductivity, corrosion-resistance, and biological affinity [24–27]. In previous works, the graphene-assembled film (GAF), with conductivity up to 10^6 S/m, has been reported and applied to antennae designs in microwave and millimeter-wave frequency bands, such as dipole antennae, wearable antennae, and conformal antennae [28–32]. These works demonstrate that GAF is characterized by a high conductivity and flexibility, is lightweight, and has mechanical stability. However, studies on the chemical stability of GAF in RF devices are still scarce. Meanwhile, the application of GAF in complex and integrated antennae needs further research. Therefore, studying the application of GAF in reconfigurable filtering antennae is of practical significance to reduce the environmental impact on antennae and extend the service life of highly integrated RF devices.

In this paper, a reconfigurable filtering antenna based on GAF is proposed. The GAF-based antenna achieves frequency switching between the UWB state and the 3.5 GHz NBF state using reconfigurable feeding networks and two PIN diodes. The operating frequency bands of the UWB state and NBF state of the GAF antenna covers 2.8–11 GHz and 3.23–3.77 GHz, respectively, with the maximum gain of 1.19–4.32 dBi and 2.32 dBi. Meanwhile, the proposed GAF-based antenna maintains good physical appearance and electrical performance in the salt spray test for two weeks. All experimental results show that the designed reconfigurable filtering antenna based on GAF has a stable impedance and radiation characteristics. Additionally, this work verifies the possibility for the multi-functional filtering antenna to achieve corrosion-resistance without other methods of metal protection.

2. Materials and Feasibility

2.1. Preparation of GAF

The precursor graphene oxide (GO) films were fabricated by casting GO gels onto a PET film, and then letting them dry in ambient conditions. Heat treatments were performed on the GO films successively up to 2850 °C. Firstly, the GO films were heated to 1300 °C with a heating rate of 3 °C/min, and then heated again to 2850 °C with a heating rate of 5 °C/min. The samples were finally roller compressed under 300 MPa to obtain density GAF.

2.2. Characterization

The transmission electronic microscopic (TEM) images of graphene oxide (GO, Figure 1a) were taken by high-resolution transmission electron microscopy (HRTEM, JEM-2100F (Japan Electronics Corporation (JEOL), Japan)). The morphology of the transparent GO nanosheets exhibited folds under thermodynamic action. This was further demonstrated by homogeneously dispersed GO nanosheets with a single atom layer, as shown in Figure 1b,c under an atomic force microscope (AFM, Asylum research Cypher ES (AsylumResearch, the United States of America (U.S.A.))), which is in favor of the high-quality preparation of GAF. The thickness of GO is 1.3 nm, which is the same as [33], with a slight deviation being the surface containing oxygen functional groups. The as-prepared GAF was depicted in Figure 1d, demonstrating a high flexibility and metallic lustre, which indicates that GAF can be used for the preparation of conformal antennae. The cross-sectional microstructure of the GAF was taken on a field-emission scanning electron microscope (SEM, JSM-7610F Plus (Japan Electronics Corporation (JEOL), Germany)) at an accelerating voltage of 5 kV. Figure 1e is the cross-sectional SEM image, indicating that the GAF, with the thickness of 25 μm , has an orderly multilayer stacked structure. The honeycomb structure of GAF nanosheets prepared by ultrasonic stripping suggests the high graphitization degree of GAF, as shown in Figure 1f. The strong peak of GAF (002) at around 26.5° (X-ray diffraction (XRD) pattern in Figure 1g), coupled with the intense G band in the GAF Raman spectra, further demonstrates the high crystallization degree of GAF [34,35]. XRD was collected on a Rigaku Smartlab using Cu $K\alpha$ ($\lambda = 1.5406 \text{ \AA}$) radiation. The Raman spectra were collected on a confocal Witec spectrometer with 532 nm excitation. The Raman spectroscopy of GAF shows D and G peaks at 1347 cm^{-1} and 1584 cm^{-1} , respectively, with the intensity ratio of the D peak and G peak of GAF indicated $I_D/I_G =$ ratio of 0.015. These results suggest that GAFs have high graphitic structures and low defect concentration. In addition, owing to the ultrahigh stability of covalent crosslinking of the sp^2 hybridized carbon atoms, the GAF exhibits excellent corrosion-resistance [33,36]. However, copper is unstable and susceptible to oxidation since its surface forms a compound by absorbing oxygen or water from the air [20]. One week after the salt spray test, the GAF maintains good physical properties, while the copper surface is severely corroded, as shown in Figure 1h. Moreover, as shown in Figure 1i, the quality of the GAF and copper with an area of $40 \text{ mm} \times 40 \text{ mm}$ is tested. The density of the GAF is 1.55 g/cm^3 , which is one fifth of the copper foil with the density of 8.64 g/cm^3 . The lightweight GAF can effectively reduce the burden of the RF front-end, providing great advantages in wearable and miniaturized electronic devices.

2.3. Feasibility

Power loss is one of the parameters that must be considered in microwave equipment, so the conductivity of the conductor material plays an important role in the performance of RF devices. The losses of the microstrip lines are mainly due to radiation loss, dielectric loss, and conductor loss. Among these three losses, the conductivity of the conductor material mainly affects the conductor loss. In the microwave RF band, in addition to the loss of the microstrip line, attention should be paid to the ground plane resistance and the propagation of the slow wave. Considering the above factors, Formulas (1)–(4) are adopted to calculate the conductor loss α_c at different conductivities,

$$\alpha_c = \frac{R}{2Z_0} \quad (1)$$

$$R = \frac{1}{2\sigma Z_0} \left[\left(\frac{1}{tw_f} \right)^p + \left[\frac{1}{\delta} \left(\frac{1}{w_f} + \frac{1}{w_f + 2\pi h e^{-\alpha_t K_\alpha 2\pi h}} \right) \right]^p \right]^{1/p} \quad (2)$$

$$\delta = \sqrt{\frac{2}{\omega\sigma\mu}} = \frac{1}{\sqrt{\pi f\mu\sigma}} \quad (3)$$

$$\alpha_t = \sqrt{\beta_z^2 - k_0^2} \quad (4)$$

where R is the resistance of the microstrip line, Z_0 is the characteristic impedance of the microstrip line with a width of w_f , σ is the conductivity, δ is the skin depth, ω is the angular frequency, t is the thickness of the conductor strip, f is the frequency, μ is the permeability, h is the thickness of the dielectric substrate, α_t is the transverse attenuation factor, β_z is the slow wave propagation constant, k_0 is the free space wave number, K_a and p are the correction factors, which are taken as 30 and 5, respectively.

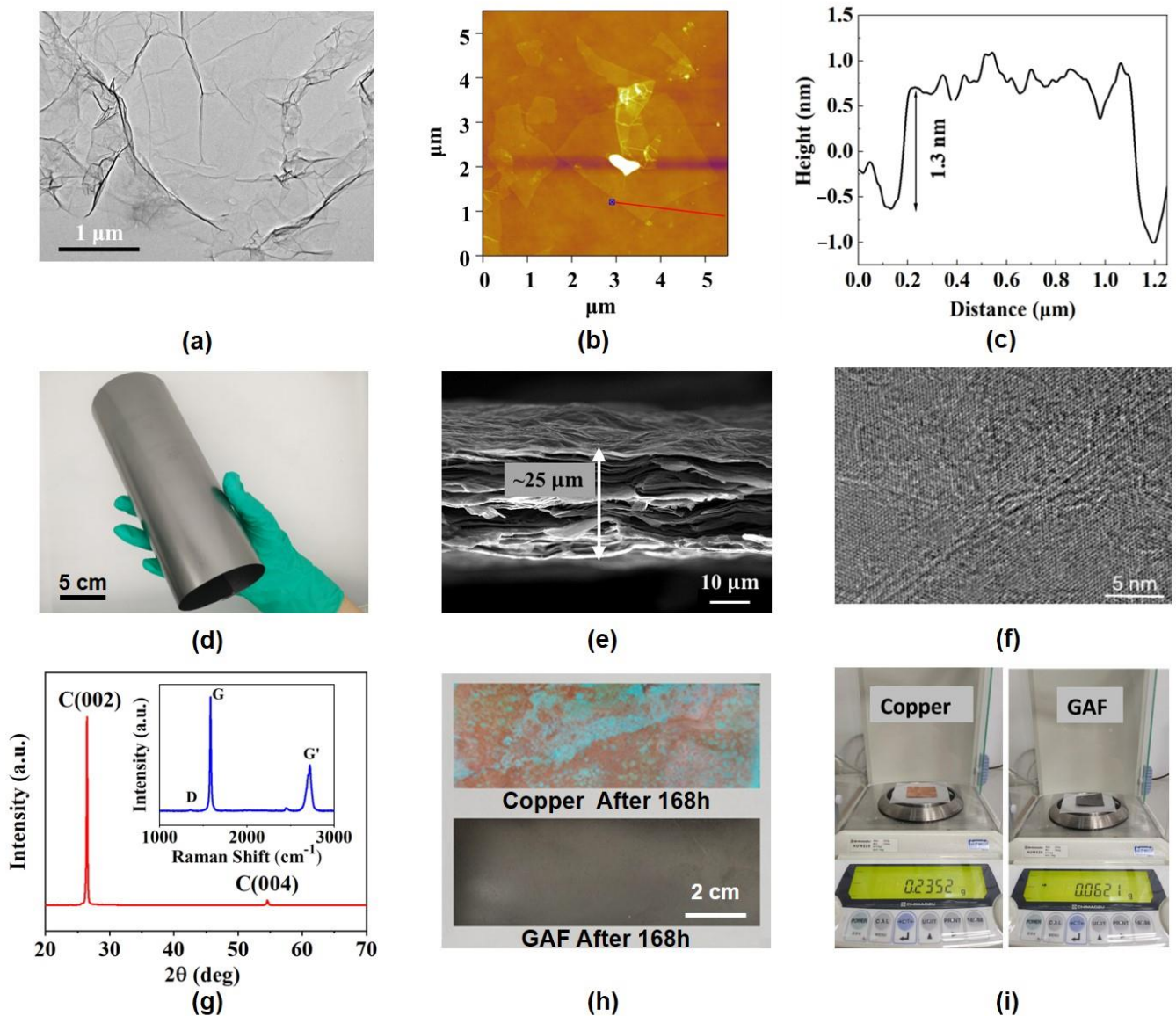


Figure 1. Characterizations and advantages of application in antenna of the GAF. (a) A typical TEM image of GO nanosheets. (b) An AFM tapping mode image of GO nanosheets deposited on a silicon substrate. (c) The corresponding height profiles of GO nanosheets measured along the red line in the AFM image. (d) A digital photo of the GAF. (e) A typical cross-sectional SEM image of the GAF with highly in-plane oriented structure. (f) A typical TEM image of GAF nanosheets prepared by ultrasonic stripping. (g) The XRD pattern of GAF and the inset shows Raman spectra of GAF. (h) Comparison of corrosion-resistance of GAF and copper. (i) The quality of GAF with 25 μm and copper with 17 μm .

Figure 2 shows the simulated relationship between the conductor loss and the conductivity of a $50\ \Omega$ microstrip line with a width of 2.54 mm at 3.5 GHz. The conductor loss α_c of the feeding line is inversely proportional to the conductivity to the power of half, according to the Formulas (1)–(4). When the conductivity is between 10^4 and 10^5 S/m, the conductor losses are large, with values of 1.9 dB/cm and 0.28 dB/cm, respectively. When the conductivity is between 10^6 – 10^7 S/m, the conductor losses tend to approximate 0.08 dB/cm and 0.03 dB/cm, respectively. Therefore, it is feasible for the GAF with a conductivity of 1.1×10^6 S/m to replace metal as the conductor material to design filtering antennae.

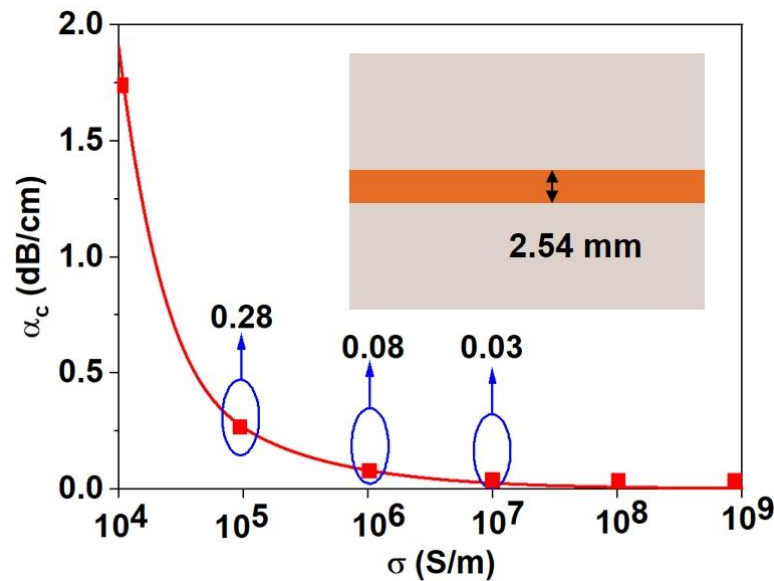


Figure 2. Relationship between conductor loss and conductivity of microstrip line.

3. Verification and Results Discussion

3.1. Design and Results of GAF-Based UWB Antenna

To obtain a wider frequency band, a circular monopole antenna, as shown in Figure 3a, is chosen as the base structure of the UWB antenna. The proposed UWB antenna is designed by introducing rectangular slots and branches on the circular monopole and making a curved modification to the upper edge of the ground. The structure and parameters of the designed UWB antenna are presented in Figure 3b. The conductor material of the UWB antenna consists of the top layer and bottom layer, which is made of the GAF (Figure 3c). The conductor layer (GAF) and the dielectric layer (Rogers 5880) are compounded together by hot pressing [37]. The top layer of the UWB antenna is a modified circular-shape monopole patch excited by a $50\ \Omega$ microstrip feeding line, and the bottom layer is the ground plane. The GAF is attached to a 0.787 mm-thick Rogers 5880 substrate with a relative permittivity (ϵ_r) of 2.2 and a loss tangent of 0.0004. The optimized UWB antenna has good impedance matching and radiation characteristics at 3.1–11 GHz, which is better than the initial monopole antenna, as shown in Figure 3d. The addition of slots and branches introduces capacitive and inductive matching for the antenna, and the curved improvement on the upper edge of the ground makes the impedance transformation of the antenna smoother, which provides a good matching impedance for the antenna over a wide-frequency band.

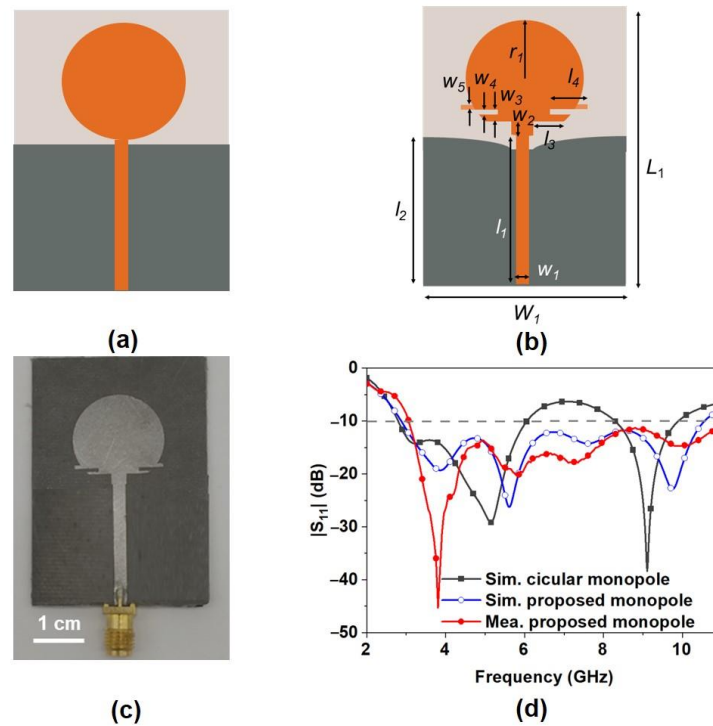


Figure 3. Structure and performance of the designed GAF-based UWB antenna. (a) Layout of the circular monopole. (b) Layout of the UWB antenna. (c) Digital photos of the GAF-based UWB antenna. (d) Reflection of the GAF-based circular monopole and the designed GAF-based UWB antenna. (Parameters: $L_1 = 50$, $W_1 = 35$, $l_1 = 23.98$, $l_2 = 26.4$, $l_3 = 4.43$, $l_4 = 4.45$, $w_1 = 2.54$, $w_2 = 2.08$, $w_3 = 0.7$, $w_4 = 0.8$, $w_5 = 0.72$, $r_1 = 9.1$. unit: mm).

3.2. Design and Results of GAF-Based Bandpass Filter

To obtain excellent filtering characteristics for the antenna, a bandpass filter is designed with the coupled feeding technology. To reduce the size and improve the flexibility, the filter is designed as a two-order stepped impedance folded ring resonator (SIFRR). The SIFRR consists of a stepped impedance resonator (SIR) folded into a ring. The physical dimensions of the filter can be determined by the following formulas. From the open circuit condition, input impedance Z_{in} can be obtained as

$$Z_{in} = jZ_1 \frac{Z_1 \tan\theta_1 \tan\theta_2 - Z_2}{Z_1 \tan\theta_2 + Z_2 \tan\theta_1} \quad (5)$$

$$Z_{in} = R_{in} + jX_{in} \quad (6)$$

the resonance condition of SIR is

$$X_{in} = 0 \quad (7)$$

Then

$$R_Z = \frac{Z_2}{Z_1} = \tan\theta_1 \tan\theta_2 \quad (8)$$

$$l = \theta \frac{c}{f_0 \sqrt{\epsilon_{re}} 2\pi} \quad (9)$$

In the SIR, Z_1 , Z_2 , θ_1 and θ_2 are the impedance and electrical length of the part of the high impedance and the low impedance, respectively. From the above formulas, the resonant frequency f_0 of the SIR is jointly determined by Z_1 , Z_2 , θ_1 and θ_2 . R_Z is the impedance ratio, the value of which can be adjusted to control the high harmonic frequency of SIR. In the above equation, l is the length of the microstrip line, ϵ_{re} is the effective

dielectric constant and the speed of light $c = 3.0 \times 10^8$ m/s. Considering the conductor loss of the microstrip line, the width of the GAF strip should not be too thin. Firstly, the impedance and length of the low impedance part and R_Z are determined to be 32Ω and 2.75, respectively, and the impedance and length of the high impedance part can be obtained as 88Ω and 13.06 mm, respectively, through Formulas (5)–(9). Then, due to the discontinuity of the microstrip lines resulting from folding, it is necessary to optimize by simulation after calculating the values of the filter.

The construction of GAF-based bandpass filter is shown in Figure 4a. The conductor strip and ground are made of GAF, as shown in Figure 5a. The substrate is Rogers 5880 with a thickness of 0.787 mm and ϵ_r of 2.2. Figure 4b explores the effect of various conductivities σ on the insertion loss of the GAF-based bandpass filter. The values of conductivity are set to 10^7 S/m, 10^6 S/m, 10^5 S/m, 10^4 S/m, 10^3 S/m. It can be seen that the decrease in σ will increase the insertion loss of the bandpass filter. When the conductivity is 10^3 S/m, 10^4 S/m and 10^5 S/m, the insertion loss of the bandpass filter deteriorates sharply at 3.5 GHz, which is 27.95 dB, 11.07 dB and 4.13 dB, respectively. However, when the conductivity is 10^6 S/m and 10^7 S/m, the corresponding insertion loss is 1.49 dB and 0.61 dB, respectively, and the difference is only 0.88 dB.

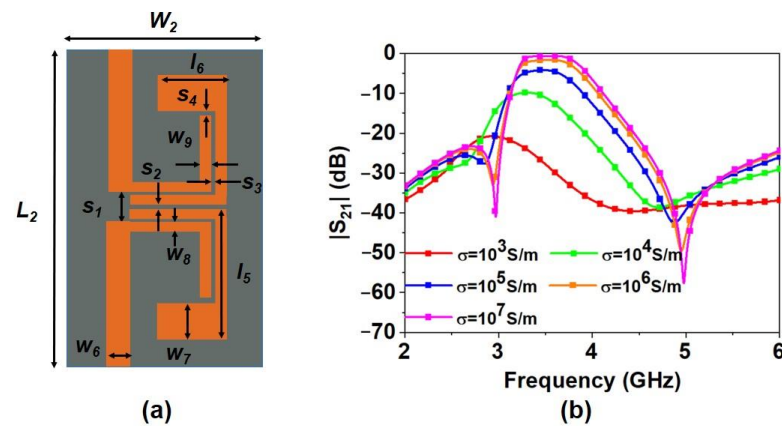


Figure 4. (a) Structure diagram of the SIFRR filter. (b) The curves of S_{21} with various conductivities. (Parameters: $L_2 = 42$, $W_2 = 25$, $l_5 = 9$, $l_6 = 7$, $w_6 = 2.54$, $w_7 = 4.5$, $w_8 = 0.87$, $w_9 = 0.87$, $s_1 = 2.64$, $s_2 = 0.3$, $s_3 = 0.3$, $s_4 = 0.3$. unit: mm).

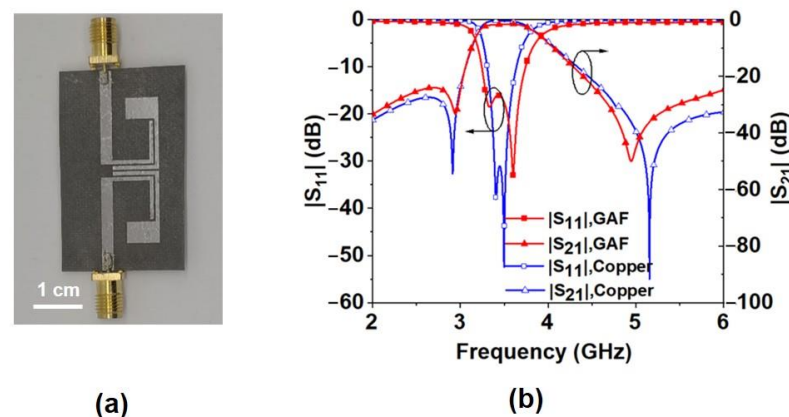


Figure 5. (a) Digital photo of the GAF-based SIFRR filter. (b) S-parameters of SIFRR filter using GAF and copper.

Based on the above simulation and analysis, the performance of the GAF-based and copper-based bandpass filter with the same structure is explored and compared in Figure 5b. The bandwidth of the GAF-based filter is 3.3–3.77 GHz with the insertion loss of 1.37 dB.

In addition, the two transmission zeros of the GAF-based filter are located at 3.06 GHz and 4.86 GHz, respectively. By comparison, the insertion loss of the GAF-based filter and copper-based filter is comparable. Furthermore, the GAF-based filter has a wider bandwidth and closer zero position than the copper-based filter. Therefore, GAF is capable of replacing metal materials for the design of bandpass filters.

3.3. Design and Results of GAF-Based Reconfigurable Filtering Antenna

Based on the above GAF-based UWB antenna and bandpass filter, the GAF-based reconfigurable filtering antenna is designed by using the dual-ports and the control function of the diodes, as shown in Figure 6. The conductor strip and ground of the reconfigurable filtering antenna are made of GAF. The substrate is also Rogers 5880 with a thickness of 0.787 mm and ϵ_r of 2.2. Two SMP1320-079LF diodes (Dio-1 and Dio-2) are selected to obtain the function of frequency reconfiguration. The equivalent circuit of the diode under the condition of forward bias and reverse bias is shown in Figure 6b, where $R_S = 0.9 \Omega$, $L_S = 0.7 \text{ nH}$, $C_T = 0.18 \text{ pF}$. When the diode is forward biased, it is equivalent to the series connection of R_S and L_S , which can be regarded as a short circuit. On the other hand, at the reverse state, the diode is considered an open circuit because it is equivalent to L_S and C_T in series. To verify the working mechanism of the proposed reconfigurable filtering antenna, CST Studio Suite 2021 was employed to simulate and analyze the antenna model. It is observed from Figure 6 that Port 1 and Port 2 of the antenna are controlled by Dio-1 and Dio-2, respectively, to achieve the switching between the UWB state and the NBF state. When Port 1 is excited (Dio-1 is turn on and Dio-2 is turn off), the GAF-based reconfigurable filtering antenna works in the UWB state. When Dio-2 is turned on and Dio-1 is turned off, it can be observed that the GAF-based antenna operates in the NBF state.

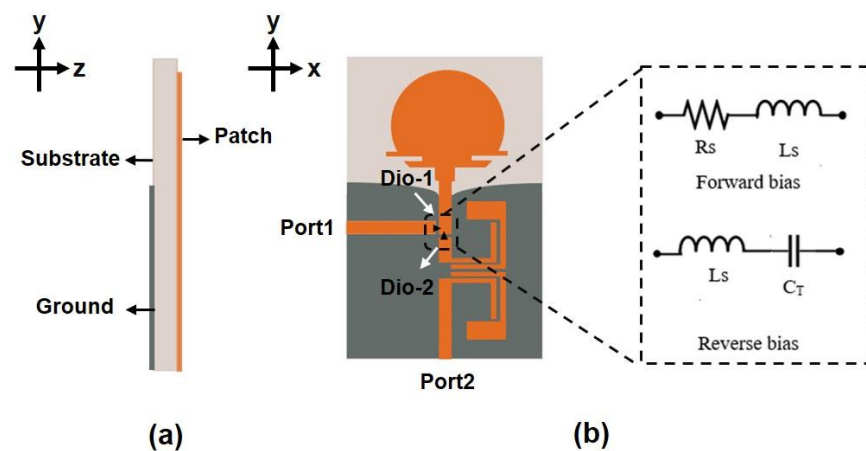


Figure 6. Configuration of proposed reconfigurable filtering antenna: (a) Side view; (b) Top view and equivalent circuits for pin diode.

The simulated current distributions in the UWB state and the NBF state at different frequencies are illustrated in Figure 7. The current is mainly distributed on the input feeding line of Port 1 and monopole patch at 3.5 GHz and 5 GHz, confirming that the antenna has good radiation characteristics over the entire frequency band of the UWB state. When Port 2 of the GAF-based reconfigurable filtering antenna is excited, there is a strong current distribution at the edge of the monopole patch at 3.5 GHz and no energy is transmitted to the antenna radiator at 5 GHz, which indicates that the reconfigurable filtering antenna has good frequency selectivity.

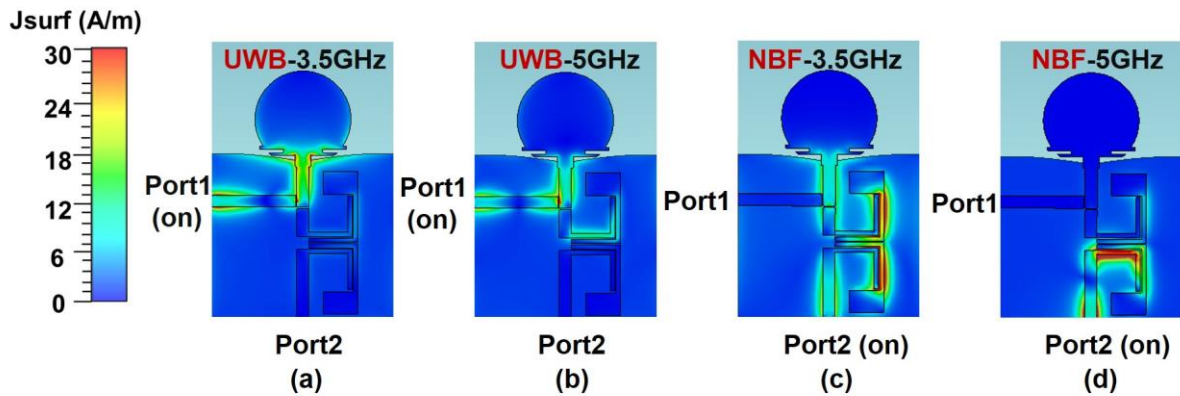


Figure 7. Surface current distributions at: (a) 3.5 GHz in UWB state; (b) 5 GHz in UWB state; (c) 3.5 GHz in NBF state; (d) 5 GHz in NBF state.

After simulation, the GAF-based reconfigurable filtering antenna is fabricated and measured. For comparison, a copper-based antenna with the same structure is also fabricated and measured. Figure 8 shows the digital photo of the GAF-based antenna with two ports and diodes. The measured bandwidth of the GAF-based antenna is 2.82–11 GHz, as shown in Figure 9a, which can completely cover the bandwidth of the UWB. It can be observed from Figure 9b that the measured bandwidth of the GAF antenna is 3.3–3.7 GHz in the NBF state. In addition, the bandwidth of the copper-based antenna is 2.88–11 GHz and 3.3–3.7 GHz in the two states, which is similar to those of the GAF-based antennae. Due to the errors of fabrication and a slight difference between the values of actual operation and the values given in the datasheet of diodes, it is reasonable and acceptable that the measured results are slightly different from the simulation results.

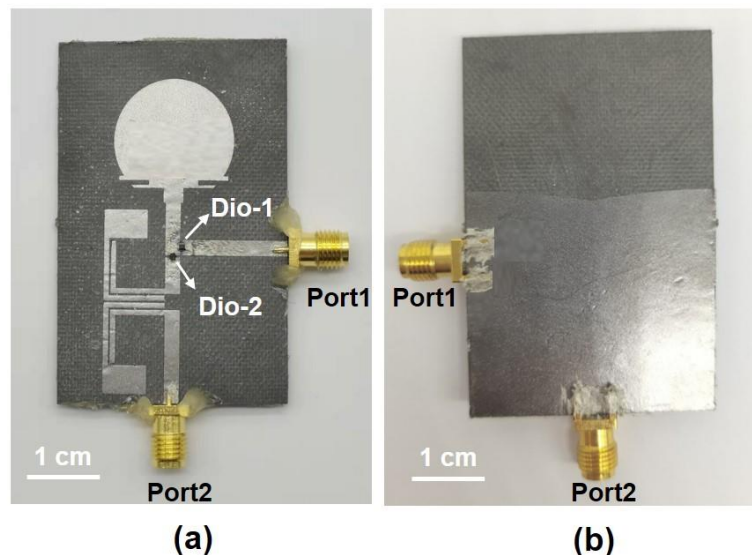


Figure 8. Digital photo of the fabricated GAF-based reconfigurable filtering antenna: (a) Top view; (b) Bottom view.

Furthermore, the measured realized gain of the proposed GAF-based antenna and copper-based antenna in the two states are shown in Figure 10a. The realized gain of the GAF-based antenna varies from 1.19–4.32 dBi in the UWB state. When the proposed antenna operates at a 3.5 GHz NBF state, the realized gain is flat up to 2.32 dBi and the out-of-band radiation suppression level is more than 25 dB. It is obvious that the GAF-based antenna has similar gain in the UWB state and the NBF state compared to the copper-based

antenna, which proves the feasibility of the GAF for the fabrication of filtering antenna. Moreover, as shown in Figure 10b, the measured port isolation of the proposed GAF-based antenna is more than 23 dB at 2–11 GHz, which is better than the copper-based antenna.

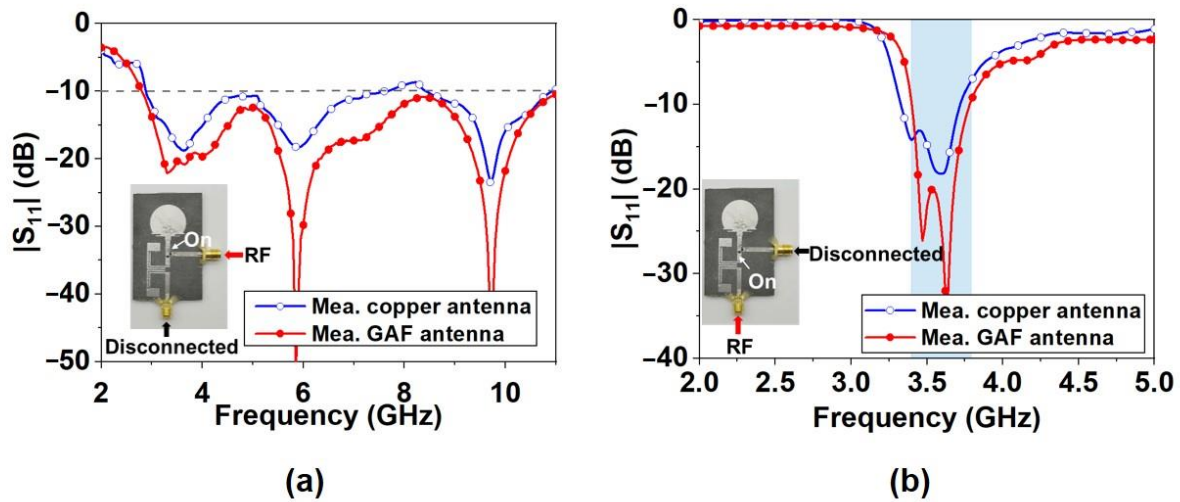


Figure 9. The measured reflection coefficients in (a) UWB state and (b) 3.5 GHz NBF state.

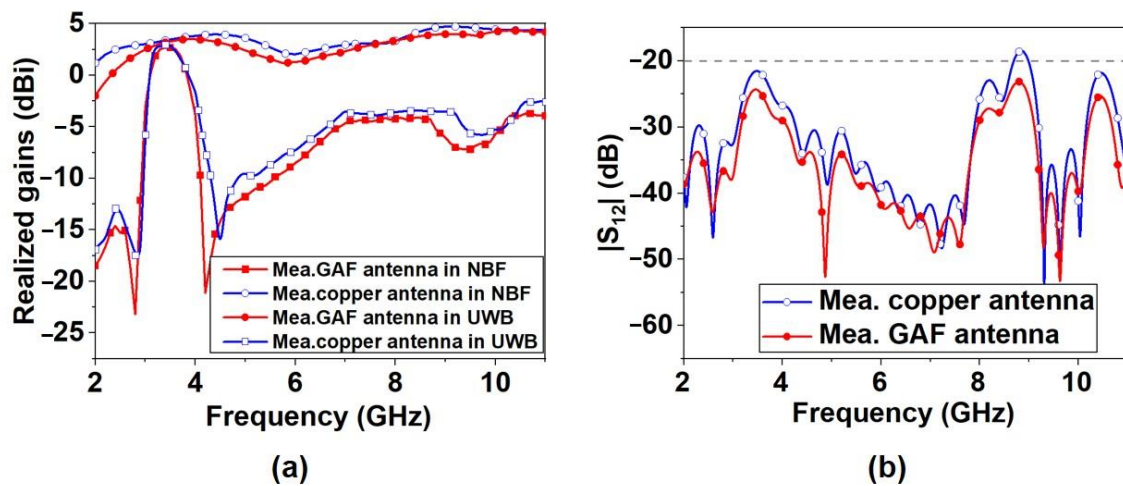


Figure 10. (a) Realized gain and (b) port isolation of the proposed antenna.

The simulated and measured radiation patterns of the GAF-based reconfigurable filtering antenna at different frequency points are displayed in Figure 11. In the UWB state, the radiation patterns are “8”-shaped and nearly omni-directional at lower frequencies in xoy plane and $yo z$ plane, respectively. The deterioration at 9 GHz is due to the excitations of high order resonance modes at high frequencies. In general, the radiation patterns in the UWB state are like that of a conventional monopole antenna, because the frequency reconfiguration achieved by adding diodes to the feeding line does not greatly affect the current distributions on the monopole patch. In the NBF state, the GAF-based antenna has similar radiation patterns to the monopole antenna at 3.5 GHz. In addition, the measured results are in agreement with the simulated ones.

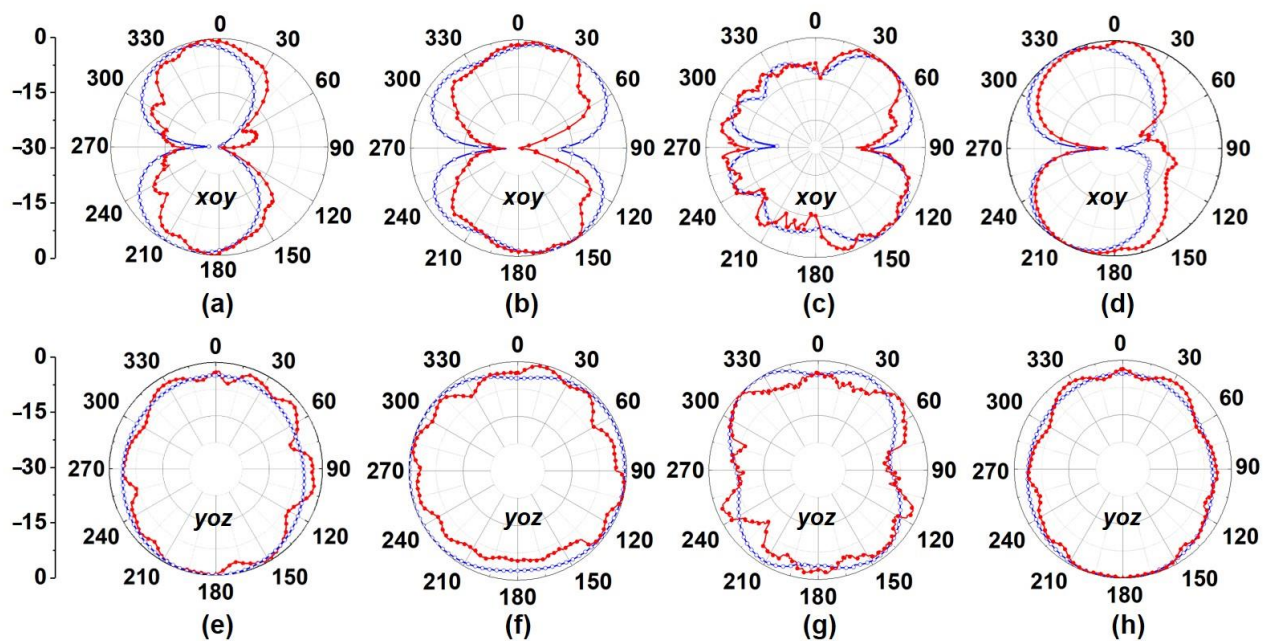


Figure 11. Simulated and measured normalized radiation patterns. (a) 3.5 GHz, xoy plane (UWB state); (b) 6 GHz, xoy plane (UWB state); (c) 9 GHz, xoy plane (UWB state); (d) xoy plane (3.5 GHz NBF state); (e) 3.5 GHz, $yozy$ plane (UWB state); (f) 6 GHz, $yozy$ plane (UWB state); (g) 9 GHz, $yozy$ plane (UWB state); (h) $yozy$ plane (3.5 GHz NBF state).

3.4. Corrosion-Resistance

To further investigate the characteristics of the proposed GAF-based antenna, the corrosion-resistance of the antennae is tested. The GAF-based antenna and copper-based antenna are put in a salt spray chamber with a standard salt spray test environment, and the corrosion states of their surfaces were detected after 168 h and 336 h. The antennae are suspended from its test surface at a distance of 15° to 25° , perpendicular to the vertical line and parallel to the main direction of the salt spray flow. The conditions of the salt spray test followed GB/T10125-2012, in which the concentration of the sodium chloride solution is 5% and the test temperature is 35 degrees Celsius. In Figure 12a, it can be seen that the surface of the GAF-based antenna is no different from than the salt spray test, while after 168 h, verdigris appears on the copper-based antenna. After 336 h, the dark brown patina spread all over the copper-based antenna, but the GAF-based antenna still retains its original physical characteristics, as shown in Figure 12b, indicating that the GAF-based antenna has better corrosion-resistance than the copper-based antenna. In addition, to further verify the performance of the copper-based antenna and the GAF-based antenna after the 336 h salt spray test, the reflection coefficients of the two antennae are tested in the UWB state and the NBF state. As can be seen from Figure 12c,d, the GAF-based antenna in both states remains in good performance, while the performance of the copper-based antenna deteriorates greatly. The test results show that the GAF-based antenna has excellent corrosion-resistance.

Moreover, the performances of the GAF-based reconfigurable filtering antenna and other antennae in references are compared, as listed in Table 1. Compared with the existing reconfigurable filtering antenna, the proposed GAF-based reconfigurable filtering antenna not only has comparable gain and bandwidth, but also has closer radiation zeros in the NBF state. In addition, the proposed GAF-based reconfigurable filtering antenna has excellent characteristics of corrosion-resistance, which are not possessed by traditional metal reconfigurable filtering antennae.

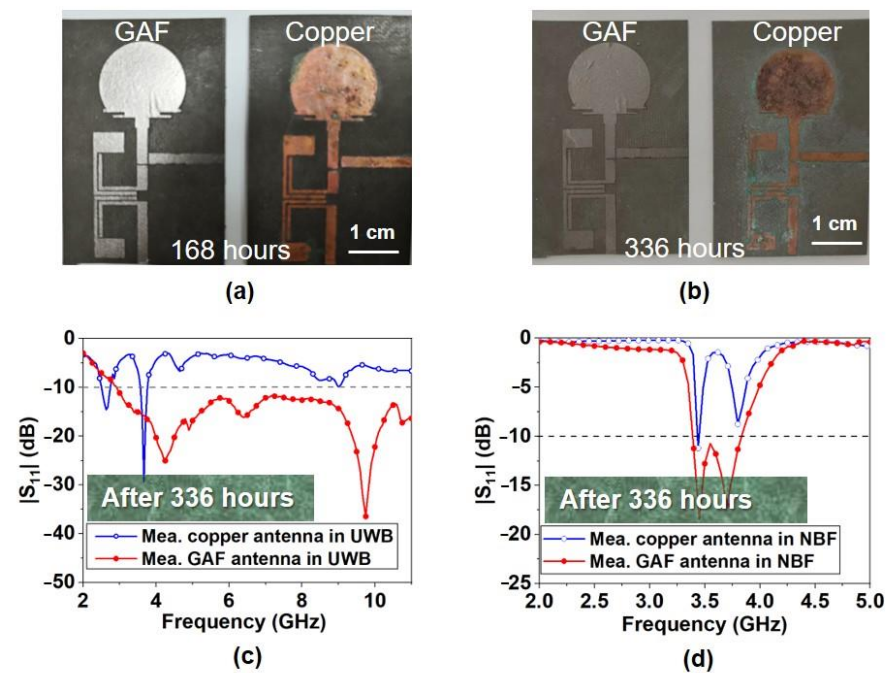


Figure 12. Comparisons of the GAF-based antenna and copper-based antenna after salt spray test. The corrosion states of surfaces of GAF-based antenna and copper-based antenna were detected after (a) 168 h and (b) 336 h. Reflection coefficients in (c) UWB state and (d) 3.5 GHz NBF state after 336 h salt spray test.

Table 1. Comparison of proposed GAF-based antenna with existing reconfigurable filtering antennae.

Ref.	Materials	Dimensions	Working Bandwidth	Average Gain (dBi)	The Position of Radiation Zero	Corrosion Resistance Property
[6]	Matal	40 mm × 38 mm	2–11 GHz (138.5%) 2.2–2.48 GHz (12.0%) 5.6–6 GHz (6.9%)	UWB: 1.01–2.28 dBi 2.4 GHz: 0.96–1.1 dBi 5.8 GHz: 1.18–1.72 dBi	–	–
[7]	Matal	8.6 mm × 24.6 mm	4.88–5.51 GHz (12.1%) 5.04–6.32 GHz (22.5%)	5.2 GHz: 1.21 dBi 5.5 GHz: 2.32 dBi	5.5 GHz: 4.41 GHz and 6.36 GHz	–
[8]	Matal	63 mm × 26 mm	3.8–6 GHz (45.0%) NB: —	WB: 3–4.1 dBi NBF: 2.3–3.8 dBi	–	–
[9]	Matal	45 mm × 40 mm	2–11 GHz (138.5%) 2.4–2.6 GHz (8%) 5–6.2 GHz (21.4%)	UWB: 0.9–1.8 dBi 2.4 GHz: 1 dBi 5.8 GHz: 1.56 dBi	–	–
This work	GAF	35 mm × 55 mm	2.88–11 (117.0%) 3.31–3.71 (11.4%)	UWB: 1.19–4.32 3.5 GHz: 2.32	3.5 GHz: 2.83 and 4.21	Good

4. Conclusions

In conclusion, we developed a GAF-based reconfigurable filtering antenna with durable corrosion-resistance and comparable radiation performances compared with the commercial copper-based antenna. The GAF-based antenna can flexibly switch between the UWB (2.8–11 GHz) and NBF (3.23–3.77 GHz) states. The realized gain of the proposed antenna varies from 1.19–4.32 dBi in the UWB state and is flap up to 2.3 dBi in the NBF state. Additionally, the port isolation of the GAF-based reconfigurable filtering antenna reaches 23 dB. Benefiting from the chemical stability of the GAF, the GAF-based antenna maintained reliable impedance and radiation performance after the 336 h salt spray corrosion test. On the contrary, the copper-based antenna performance exhibited rapid degradation under salt spray corrosion. This research is of great significance to improve the reliability, electrical performance, and life cycle of the antennae in harsh environments.

Author Contributions: Conceptualization, H.Z. and R.S.; Methodology, C.T., R.S. and D.H.; Software, Y.H.; validation, H.F., H.Z., B.W., G.-L.H., Z.K. and K.L.; Investigation, Y.H., R.S. and X.C.; Writing—original draft preparation, Y.H., H.Z. and R.S.; Supervision, D.H.; Funding acquisition, D.H. All authors have read and agreed to the published version of the manuscript.

Funding: This research was funded by the National Natural Science Foundation of China Grant No. 51672204, 51701146, 62001338, the Fundamental Research Funds for the Central Universities No. WUT: 2020IB005, 205209016 and 2019IB017.

Data Availability Statement: Data is contained within the article.

Conflicts of Interest: The authors declare no conflict of interest.

References

1. Mao, C.; Gao, S.; Wang, Y.; Liu, Y.; Yang, L.; Cheng, Z.; Geng, Y. Integrated dual-band filtering/duplexing antennas. *IEEE Access* **2018**, *6*, 8403–8411. [\[CrossRef\]](#)
2. Jin, J.Y.; Liao, S.; Xue, Q. Design of filtering-radiating patch antennas with tunable radiation nulls for high selectivity. *IEEE Trans. Antennas Propag.* **2018**, *66*, 2125–2130. [\[CrossRef\]](#)
3. Mao, C.X.; Gao, S.; Wang, Y.; Sanz-Izquierdo, B.; Wang, Z.; Qin, F.; Chu, Q.X.; Li, J.; Wei, G.; Xu, J. Dual-band patch antenna with filtering performance and harmonic suppression. *IEEE Trans. Antennas Propag.* **2016**, *64*, 4074–4077. [\[CrossRef\]](#)
4. Lin, X.; Xie, Z.; Zhang, P.; Zhang, Y. A broadband filtering duplex patch antenna with high isolation. *IEEE Antennas Wirel. Lett.* **2017**, *16*, 1937–1940. [\[CrossRef\]](#)
5. Hu, P.F.; Pan, Y.M.; Zhang, X.Y.; Zheng, S.Y. Broadband filtering dielectric resonator antenna with wide stopband. *IEEE Trans. Antennas Propag.* **2017**, *65*, 2079–2084. [\[CrossRef\]](#)
6. Deng, J.; Hou, S.; Zhao, L.; Guo, L. Wideband-to-narrowband tunable monopole antenna with integrated bandpass filters for UWB/WLAN applications. *IEEE Antennas Wirel. Lett.* **2017**, *16*, 2734–2737. [\[CrossRef\]](#)
7. Deng, J.; Hou, S.; Zhao, L.; Guo, L. A reconfigurable filtering antenna with integrated bandpass filters for UWB/WLAN applications. *IEEE Trans. Antennas Propag.* **2018**, *66*, 401–404. [\[CrossRef\]](#)
8. Fakharian, M.M.; Rezaei, P.; Orouji, A.A.; Soltanpur, M.A. A wideband and reconfigurable filtering slot antenna. *IEEE Antennas Wirel. Lett.* **2016**, *15*, 1610–1613. [\[CrossRef\]](#)
9. Qin, P.; Wei, F.; Guo, Y.J. A wideband-to-narrowband tunable antenna using a reconfigurable filter. *IEEE Trans. Antennas Propag.* **2015**, *63*, 2282–2285. [\[CrossRef\]](#)
10. Jin, Z.H.; Ge, H.H.; Lin, W.W.; Zong, Y.W.; Liu, S.J.; Shi, J.M. Corrosion behaviour of 316L stainless steel and anti-corrosion materials in a high acidified chloride solution. *Appl. Surf. Sci.* **2014**, *322*, 47–56. [\[CrossRef\]](#)
11. Jiang, F.; Zhao, W.; Wu, Y.; Wu, Y.; Liu, G.; Dong, J.; Zhou, K. A polyethyleneimine-grafted graphene oxide hybrid nanomaterial: Synthesis and anti-corrosion applications. *Appl. Surf. Sci.* **2019**, *479*, 963–973. [\[CrossRef\]](#)
12. Tong, Y.; Bohm, S.; Song, M. The capability of graphene on improving the electrical conductivity and anti-corrosion properties of polyurethane coatings. *Appl. Surf. Sci.* **2017**, *424*, 72–81. [\[CrossRef\]](#)
13. Waqas, H.M.; Shi, D.; Imran, M.; Khan, S.Z.; Tong, L.; Ahad, F.E.; Zaidi, A.A.; Iabal, J.; Ahmed, W. Conceptual design of composite sandwich structure submarine radome. *Materials* **2019**, *12*, 1966. [\[CrossRef\]](#) [\[PubMed\]](#)
14. Kenion, T.; Yang, N.; Xu, C. Dielectric and mechanical properties of hypersonic radome materials and metamaterial design: A review. *J. Eur. Ceram. Soc.* **2022**, *42*, 1–17. [\[CrossRef\]](#)
15. Cipri, F.; Bartoli, C.; Valente, T.; Casadei, F. Electromagnetic and mechanical properties of silica-aluminosilicates plasma sprayed composite coatings. *J. Therm. Spray Technol.* **2007**, *16*, 831–838. [\[CrossRef\]](#)
16. Deya, C.; del Arno, B.; Romagnoli, R. Ceramic microspheres to improve anticorrosive performance of phosphate paints. *Ceram. Int.* **2012**, *38*, 2637–2646. [\[CrossRef\]](#)
17. Deya, C.; Blustein, G.; del Arno, B.; Romagnoli, R. Evaluation of eco-friendly anticorrosive pigments for paints in service conditions. *Prog. Org. Coat.* **2010**, *69*, 1–6. [\[CrossRef\]](#)
18. Jianhua, L.; Junxiu, S.; Songmei, L. Effects of electroplated coatings on corrosion behavior of Ti-1023/30CrMnSiA galvanic couple. *J. Wuhan Univ. Technol.* **2008**, *23*, 704–707.
19. Garcia, I.; Valdez, B.; Schorr, M.; Herrera, T.E.; Duran, J.A.; Ramirez, V. Sacrificial anodes for cathodic protection in the oil industry in Mexico. *Mater. Perform.* **2015**, *54*, 38–42.
20. Pang, J.; Blackwood, D.J. Corrosion of titanium alloys in high temperature near anaerobic seawater. *Corros. Sci.* **2016**, *105*, 17–24. [\[CrossRef\]](#)
21. Attar, H.; Prashanth, K.G.; Zhang, L.; Calin, M.; Okulov, I.V.; Scudino, S.; Yang, C.; Eckert, J. Effect of powder particle shape on the properties of in situ Ti-TiB composite materials produced by selective laser melting. *J. Mater. Sci. Technol.* **2015**, *31*, 1001–1005. [\[CrossRef\]](#)
22. Dejun, S.; Long, N.; Shengli, Y. Research on application technology of titanium alloy in marine pipeline. *Rare Met. Mater. Eng.* **2020**, *49*, 1100–1104.

23. Bai, Y.; Gai, X.; Li, S.; Zhang, L.; Liu, Y.; Hao, Y.; Zhang, X.; Yang, R.; Gao, Y. Improved corrosion behaviour of electron beam melted Ti-6Al-4V alloy in phosphate buffered saline. *Corros. Sci.* **2017**, *123*, 289–296. [[CrossRef](#)]
24. Dastgeer, G.; Shahzad, Z.M.; Chae, H.; Kim, Y.H.; Ko, B.M.; Eom, J. Bipolar junction transistor exhibiting excellent output characteristics with a prompt response against the selective protein. *Adv. Funct. Mater.* **2022**, *32*, 2204781. [[CrossRef](#)]
25. Dastgeer, G.; Afzal, A.M.; Jaffery, S.H.A.; Imran, M.; Assiri, M.A.; Nisar, S. Gate modulation of the spin current in graphene/WSe₂ van der Waals heterostructure at room temperature. *J. Alloys Compd.* **2022**, *919*, 165815. [[CrossRef](#)]
26. Duong, H.M.; Tran, T.Q.; Kopp, R.; Myint, S.M.; Peng, L. Chapter 1—Direct spinning of horizontally aligned carbon nanotube fibers and films from the floating catalyst method. In *Nanotube Superfiber Materials*, 2nd ed.; Schulz, M.J., Shanov, V., Yin, Z., Cahay, M., Eds.; William Andrew Publishing: Norwich, NY, USA, 2019; pp. 3–29.
27. Duong, H.M.; Myint, S.M.; Tran, T.Q.; Le, D.K. Chapter 6—Post-spinning treatments to carbon nanotube fibers. In *Carbon Nanotube Fibers and Yarns*; Miao, M., Ed.; Woodhead Publishing: Sawston, UK, 2020; pp. 103–134.
28. Song, R.; Wang, Q.; Mao, B.; Wang, Z.; Tang, D.; Zhang, B.; Zhang, J.; Liu, C.; He, D.; Wu, Z.; et al. Flexible graphite films with high conductivity for radio-frequency antennas. *Carbon* **2018**, *130*, 164–169. [[CrossRef](#)]
29. Tang, D.; Wang, Q.; Wang, Z.; Liu, Q.; Zhang, B.; He, D.; Wu, Z.; Mu, S. Highly sensitive wearable sensor based on a flexible multi-layer graphene film antenna. *Sci. Bull.* **2018**, *63*, 574–579. [[CrossRef](#)]
30. Zu, H.; Wu, B.; Zhang, Y.; Zhao, Y.; Song, R.; He, D. Circularly polarized wearable antenna with low profile and low specific absorption rate using highly conductive graphene film. *IEEE Antennas Wirel. Lett.* **2020**, *19*, 2354–2358. [[CrossRef](#)]
31. Song, R.; Wang, Z.; Zu, H.; Chen, Q.; Mao, B.; Wu, Z.P.; He, D. Wideband and low sidelobe graphene antenna array for 5G applications. *Sci. Bull.* **2021**, *66*, 103–106. [[CrossRef](#)]
32. Song, R.; Mao, B.; Wang, Z.; Hui, Y.; Zhang, N.; Fang, R.; Zhang, J.; Wu, Y.; Ge, Q.; Novoselov, K.S.; et al. Comparison of copper and graphene-assembled films in 5G wireless communication and THz electromagnetic-interference shielding. *Proc. Natl. Acad. Sci. USA* **2023**, *120*, e2085160176. [[CrossRef](#)]
33. Zhou, T.; Ni, H.; Wang, Y.; Wu, C.; Zhang, H.; Zhang, J.; Tomsia, A.P.; Jiang, L.; Cheng, Q. Ultratough graphene-black phosphorus films. *Proc. Natl. Acad. Sci. USA* **2020**, *117*, 8727–8735. [[CrossRef](#)] [[PubMed](#)]
34. Ebrahimi, S.; Bordbar-Khiabani, A.; Yarmand, B. Enhanced optoelectronic performance of plasma electrolytic oxidized monocrySTALLINE silicon using rGO incorporation. *Mater. Lett.* **2019**, *239*, 151–154. [[CrossRef](#)]
35. Ebrahimi, S.; Bordbar-Khiabani, A.; Yarmand, B.; Asghari, M.A. Improving optoelectrical properties of photoactive anatase TiO₂ coating using rGO incorporation during plasma electrolytic oxidation. *Ceram. Int.* **2019**, *45*, 1746–1754. [[CrossRef](#)]
36. Geim, A.K.; Novoselov, K.S. The rise of graphene. *Nat. Mater.* **2007**, *6*, 183–191. [[CrossRef](#)] [[PubMed](#)]
37. Song, R.; Zhao, X.; Wang, Z.; Fu, H.; Han, K.; Qian, W.; Wang, S.; Shen, J.; Mao, B.; He, D. Sandwiched graphene clad laminate: A binder-free flexible printed circuit board for 5G antenna application. *Adv. Eng. Mater.* **2020**, *22*, 2000451. [[CrossRef](#)]

Disclaimer/Publisher’s Note: The statements, opinions and data contained in all publications are solely those of the individual author(s) and contributor(s) and not of MDPI and/or the editor(s). MDPI and/or the editor(s) disclaim responsibility for any injury to people or property resulting from any ideas, methods, instructions or products referred to in the content.